



HAL
open science

Feasibility study of a surface-borehole NMR method

Anatoly Legchenko, Benoît Texier, Jean-François Girard, Jean-Michel Vouillamoz, Fabrice Messan Amene Lawson, Iboukoun Christian Alle, Jean-Michel Baltassat, Ghislain Pierrat, Marie Boucher

► To cite this version:

Anatoly Legchenko, Benoît Texier, Jean-François Girard, Jean-Michel Vouillamoz, Fabrice Messan Amene Lawson, et al.. Feasibility study of a surface-borehole NMR method. *Journal of Applied Geophysics*, 2020, 177, pp.104039. 10.1016/j.jappgeo.2020.104039 . hal-02913683

HAL Id: hal-02913683

<https://brgm.hal.science/hal-02913683>

Submitted on 22 Aug 2022

HAL is a multi-disciplinary open access archive for the deposit and dissemination of scientific research documents, whether they are published or not. The documents may come from teaching and research institutions in France or abroad, or from public or private research centers.

L'archive ouverte pluridisciplinaire **HAL**, est destinée au dépôt et à la diffusion de documents scientifiques de niveau recherche, publiés ou non, émanant des établissements d'enseignement et de recherche français ou étrangers, des laboratoires publics ou privés.



Distributed under a Creative Commons Attribution - NonCommercial 4.0 International License

14 **Abstract**

15 We present results of a feasibility study of a borehole induction-coil sensor for surface-
16 borehole NMR (nuclear magnetic resonance - SBNMR) investigations. This sensor of 7 cm
17 diameter and 180 cm length is connected to a standard MRS (Magnetic Resonance Sounding)
18 instrument. Thus, SBNMR is a cost-effective extension of the MRS method. Using a
19 downhole sensor increases the depth of investigation and the resolution of MRS. In the near-
20 horizontal Earth's magnetic field, the sensitive area of the sensor is represented by a cylinder
21 of a few meters in diameter. A blind zone of 0.5 to 1 m around the borehole is due to the
22 disturbance of the Earth's magnetic field by the magnetic core of the sensor. The relatively
23 large volume investigated with SBNMR and the blind zone around borehole may represent an
24 advantage of SBNMR over the NMR borehole tool investigating a narrow zone around the
25 borehole. However, using the Earth's magnetic field renders the SBNMR performance site
26 dependent with an inherently low signal-to-noise ratio. Our first results show a good
27 correspondence between SBNMR, MRS and borehole data.

28

29 **Key words:** MRS, SNMR, surface-borehole, water content, SBNMR

30

31 **Introduction**

32 Selective sensitivity to groundwater is a major advantage of geophysical methods based on
33 the phenomenon of nuclear magnetic resonance (NMR) compared to other geophysical
34 techniques. NMR-based methods can be applied in a borehole or from surface. Downhole,
35 NMR is mainly used in petroleum exploration and production (Dunn et al., 2002); as these
36 tools were initially developed for deep large-diameter boreholes, they are rarely applied to
37 groundwater investigations. However, recent advances in NMR have allowed developing
38 NMR tools adapted to the small-diameter boreholes typical of hydrogeology (Walsh et al.,
39 2013).

40 Surface NMR (SNMR), also known as Magnetic Resonance Sounding (MRS), is a non-
41 invasive geophysical method (Legchenko and Valla, 2002; Hertrich, 2008; Legchenko, 2013;
42 Behroozmand et al., 2015). MRS and borehole NMR are based on the same physical
43 phenomenon and have many common features, but these methods are not interchangeable
44 (e.g. Müller-Petke et al., 2011). The maximum depth of investigation with MRS is site
45 dependent and rarely exceeds 100 m (Legchenko et al., 1997). The resolution is also variable
46 and progressively decreases with increasing depth (e.g. Girard et al., 2007; Müller-Petke and
47 Yaramanci, 2008; Hertrich et al., 2009; Chevalier et al, 2014; Parsekian and Grombacher,
48 2015). A limited investigation depth and relatively poor resolution are the properties of MRS
49 (Legchenko and Pierrat, 2014).

50 Stoeffl (2001) proposed to improve MRS by combining surface and borehole NMR
51 methods. Using a transmitting loop on the surface and a magnetic-field sensor downhole, we
52 obtain surface-borehole NMR (SBNMR). The possibility of using with MRS a small
53 magnetic-field sensor instead of a large loop was demonstrated by Davis et al. (2014) using a
54 SQUID sensor. However, the use of a SQUID sensor for SBNMR is not absolutely necessary
55 and we developed a more traditional induction-coil sensor. Hereafter, we report the first
56 experimental results.

57 **Surface-borehole NMR**

58 Practical implementation of the SBNMR method can be done with a standard MRS
59 instrument equipped with an additional induction-coil sensor in the borehole. Figure 1 shows
60 the measuring setup consisting of a transmitting loop (Tx) on the surface and a sensor in the
61 borehole (Rx).

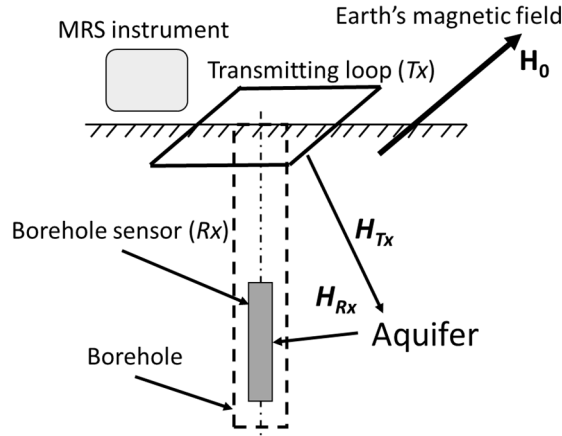


Fig. 1. Transmitting loop on the surface (Tx) and the induction-coil sensor downhole (Rx)

For measuring, a pulse of alternative current oscillating with the Larmor frequency is generated in the transmitting loop, producing the excitation magnetic field H_{Tx} . The pulse is characterized by a pulse moment being a product of the current amplitude and duration. After the pulse is terminated, groundwater generates a magnetic field H_{Rx} , which induces a voltage in the induction coil in the borehole. Both, sensor position and current magnitude in the loop can be varied. Records of the magnetic resonance signal at each combination of sensor depth and pulse moment provide data for interpretation.

Sensor design

Our sensor consists of an open-core coil with a ferrite core (Fig. 2). The coil and connecting cables are protected by electrostatic screens. The sensor is mechanically protected by a plastic tube.

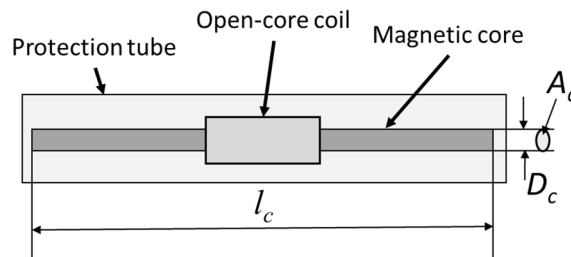


Fig. 2. Design of the borehole sensor (l_c – length of the core, D_c – diameter of the core, A_c – area of the core)

The voltage induced in a coil is given by Faraday's law:

$$V = -\mu_0 \mu_c n A_c \frac{dH}{dt}, \quad (1)$$

82 where $\mu_0 = 4\pi \times 10^{-7}$ H/m, μ_c is the resultant permeability of the core, n is a number of
 83 turns in the coil and A_c is the core cross-section area. The resultant permeability μ_c may be
 84 smaller than the core material permeability μ_r due to the demagnetizing field effect:

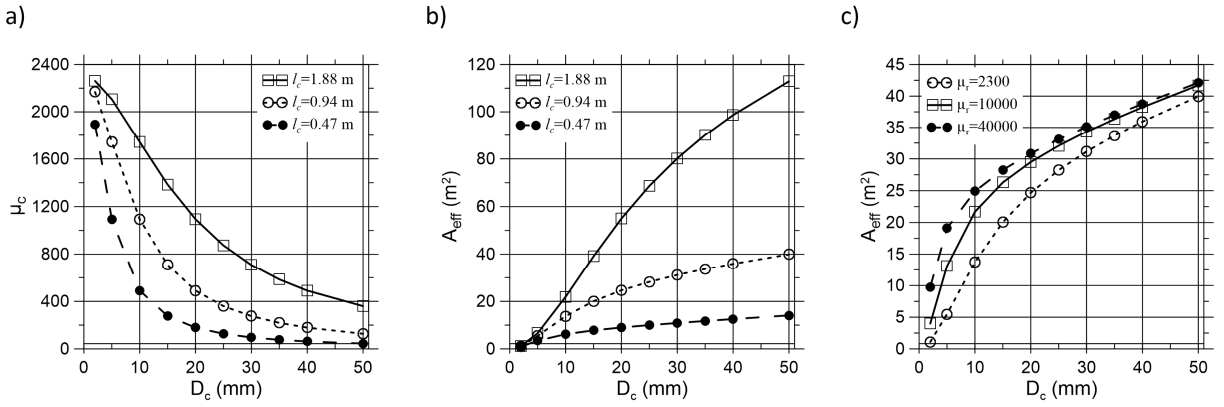
$$85 \quad \mu_c = \frac{\mu_r}{1 + N_d(\mu_r - 1)}, \quad (2)$$

86 where N_d is demagnetizing factor that is dependent on the core geometry. It can be estimated
 87 as (Tumanski, 2007):

$$88 \quad N_d \cong \frac{D_c^2}{l_c^2} \left(\ln(2l_c / D_c) - 1 \right), \quad (3)$$

89 where D_c and l_c are the diameter and length of the core, respectively.

90 Thus, the transfer function between the magnetic field and the voltage induced in the coil
 91 depends on the effective area $A_{eff} = n\mu_c A_c$ defined by the magnetic permeability of the
 92 material and the sensor geometry. For estimating the sensor parameters, we considered a
 93 ferrite core with $\mu_r = 2300$ and used Eqs. 1-3. Fig. 3a shows the resultant magnetic
 94 permeability μ_c versus core diameter and, considering different core lengths, shows that if
 95 the l_c / D_c ratio increases then $\mu_c \rightarrow \mu_r$. Fig. 3b shows the effective area versus the core
 96 diameter, and Fig. 3c demonstrates that for a fixed core length the effective area cannot be
 97 significantly increased by increasing μ_r .



98

99

100

101

102

103

104

105

106

107

108

109

110

111

112

113

114

115

116

117

118

119

120

121

Fig. 3a) The resultant magnetic permeability of the core versus core diameter computed considering different core lengths ($\mu_r=2300$). b) The effective area versus core diameter ($\mu_r=2300$). c) The effective area computed considering different magnetic-permeability values of the material and fixed core length ($l_c=0.94$ m).

Fig. 3 suggests using a long core of large diameter, but sensor dimensions are limited by practical considerations such as the borehole diameter as well as the facility of shipping and handling. To start with, we fabricated a sensor with an external diameter of 70 mm. The core ($l_c=1767$ mm) was made of ferrite bars with dimensions of $27.5 \times 30 \times 93$ mm³ and $\mu_r = 2300 \pm 20\%$ (1840 - 2760) at 25 °C. The ferrite bar geometry is guaranteed by the manufacturer with an accuracy of $\pm 2\%$. Our coil contains 160 turns and has a resistivity of 1.35 Ω ; Eqs. 1 to 3 allow computing $A_{eff} = 78.7$ m². For modelling, we can represent the sensor by a magnetic dipole with the respective surface area.

Between 0 °C and 30 °C the ferrite magnetic permeability has an almost linear temperature dependence, changing with a temperature coefficient of 0.7%/°. At 0 °C $\mu_r = 1900$ and at 30 °C it is $\mu_r = 2380$. The corresponding effective area changes from 74.7 m² to 79.4 m² (from -5% to 0.9%) with a consequent impact on the measured voltage. The uncertainty in the magnetic permeability of ferrite causes a corresponding uncertainty in the effective area from 73.9 m² to 82.3 m² (from -4.5% to 6%). Thus, without calibration, variations in core magnetic permeability can cause an uncertainty in measuring voltage of up to $\pm 6\%$.

Noise considerations

The accuracy of the signal measurements depends on the noise level. Electromagnetic noise is generated by different sources, such as the amplifier, the coil wire, the magnetic core

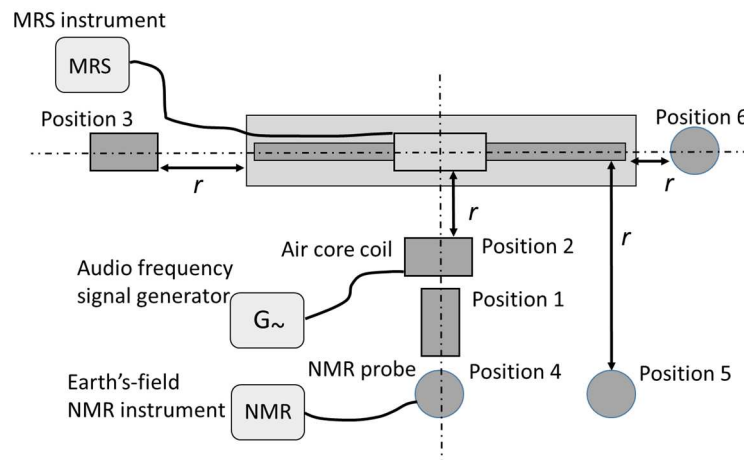
122 and several other external sources. As the core is not exposed to mechanical or magnetic
 123 stress, we exclude a noise due to the Backhausen effect as well as other possible noises
 124 generated by the ferrite core. The coil wire produces thermal noise that can be estimated as:

$$125 \quad V_T = 2\sqrt{k_B T \Delta f R}, \quad (4)$$

126 where $k_B = 1.38 \times 10^{-23}$ J/K is the Boltzmann constant, T is the temperature, Δf is the
 127 bandwidth and R is the wire resistance.

128 Considering a bandwidth of $\Delta f = 300$ Hz (NUMIS^{poly} MRS instrument), $T = 293$ °K and
 129 wire resistance $R = 1.35$ Ω, we obtain a thermal noise of 2.6 nV (0.15 nV/Hz^{-1/2}). This noise
 130 can be reduced by lowering the wire resistivity. Amplifier noise reported by MRS instrument
 131 manufacturers varies between 0.1 and 1.78 nV/Hz^{-1/2}, yielding a noise voltage varying
 132 between 1.7 and 31 nV ($\Delta f = 300$ Hz). In practice, external noise is added to amplifier noise.
 133 When using a large loop, the external noise is much larger than the amplifier noise. For
 134 example, during our MRS study on the Greenland ice sheet, far from everything (Legchenko
 135 et al., 2018), the natural external noise measured with a typical MRS loop (80×80 m²) slightly
 136 varied around 100 nV. Such noise may be several times larger during magnetic storms. In
 137 built-up areas, manmade noise can be much larger than atmospheric one. However, when
 138 using borehole sensors as well as small receiving loops (Grombacher et al., 2018), external
 139 noise voltage may be equal to or even smaller than the amplifier noise, and the amplifier
 140 design becomes an important issue.

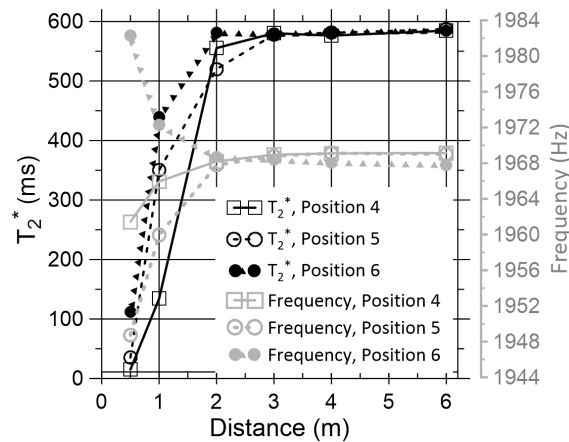
141 The borehole sensor in laboratory, for which we used an experimental setup shown in
 142 Fig. 4.



143
 144 *Fig. 4. The experimental setup for measuring parameters of the induction-coil sensor*

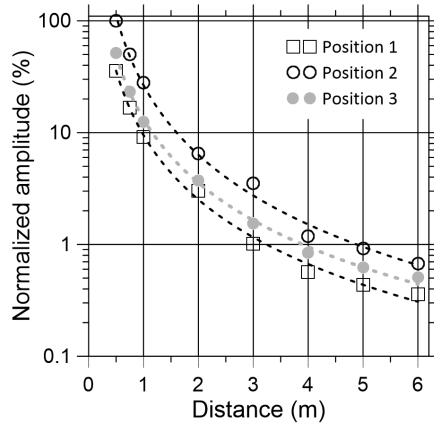
145

146 An Earth's-field NMR instrument with a water sample probe (Clément et al., 2011)
 147 evaluated the heterogeneity of the Earth's magnetic field disturbed by the sensor core. Fig. 5
 148 shows the relaxation time T_2^* and the Larmor frequency both characterizing the homogeneity
 149 of the Earth's magnetic field. Far from the sensor, the relaxation time was $T_2^*=585$ ms, the
 150 Larmor frequency being 1969 Hz. Then, the probe with the water sample was placed at
 151 different distances from the sensor (positions 4 to 6), and we measured the Larmor frequency
 152 and the relaxation time T_2^* again. At less than 50 cm, the free-induction decay signal (FID)
 153 could not be measured because of short T_2^* values; only spin-echo (SE) measurements
 154 allowed observing the NMR signal in the vicinity of the sensor. At larger distances, the FID
 155 signal was well observed. Our results show that at about 0.5 to 1 m around the sensor the FID
 156 signal is well measured, but the relaxation time is shortened and the Larmor frequency is
 157 shifted. At 1 to 2 m from the sensor, the measurements are moderately disturbed and beyond
 158 2 m the Earth's magnetic field is only slightly disturbed.



159
 160 *Fig. 5. Relaxation time T_2^* (left vertical axis) and Larmor frequency (right vertical axis)*
 161 *versus distance between sensor and water sample.*

162
 163 Then, the sensor was connected to the MRS instrument. To estimate the max radial extent
 164 of the sensitive volume, an audio-frequency generator connected to an air core coil was used
 165 for generating a test signal and the MRS instrument applied as a simple voltmeter measured
 166 voltage induced in the sensor coil. Both, generator and MRS instrument were tuned to the
 167 same frequency of 1969 Hz. We set the coil at different positions around the sensor (positions
 168 1-3) and measured voltage *versus* distance r between coil and sensor. The normalized
 169 amplitude of the signal *versus* distance is shown on Fig. 6.



170

171 *Fig. 6. Normalized amplitude of the test signal measured at different positions of the*
 172 *transmitting coil versus distance between sensor and coil. Dashed lines show the power fit of*
 173 *experimental data.*

174

175 These measurements show that voltage induced by the test coil rapidly decreased with
 176 distance and 6 m from the sensor the amplitude represented only about 0.6% of the initial
 177 value measured at 0.5 m. For each position, the measured amplitudes were fitted by a function

178 $e = a_i / r^b$ (dashed lines). For positions 1 and 3, $b = 1.9$ and for position 2, $b = 2.1$. The fitting

179 coefficient a_i has individual values for each position. These measurements showed that near

180 the real sensor, the sensitivity decreases with a rate of approximately $\sim 1/r^2$.

181 Fig. 6 shows the sensitivity of the sensor to a local signal source (air-core coil). However,
 182 the NMR signal is produced by a volume of water around the borehole, which increases as a
 183 square function of distance; therefore, the sensitive zone of the sensor can be extended beyond
 184 the estimate shown on Fig. 6. However, the volume of water that produces an NMR signal is
 185 dependent upon the excitation magnetic field generated by the transmitting loop as well as
 186 upon the inclination of the Earth's magnetic field; these parameters are site dependent and
 187 required more detailed investigations, which was outside the scope of this study.

188 **Forward modelling**

189 For measuring a magnetic resonance signal from groundwater, an alternating-current pulse
 190 with amplitude I_0 and duration τ was generated in the transmitting loop on surface. After
 191 switching off the current, the subsurface water generates an exponentially decaying magnetic

192 field that oscillates with the Larmor frequency ω_0 . The voltage induced in the measuring coil
 193 can be calculated as (Weichman et al., 2000; Hertrich et al., 2005):

$$194 \quad V(q,t) = \int K(\mathbf{r},q) \int w(\mathbf{r},T_2^*) \exp(-t/T_2^*) dT_2^* d\mathbf{r} \quad , \quad (5)$$

195 where $q = I_0 \tau$ is the pulse moment, $w(\mathbf{r},T_2^*)$ is distribution water in the subsurface and
 196 $K(\mathbf{r},q)$ is the kernel function describing spatial sensitivity. If investigating only the water
 197 content, then the initial amplitude of the magnetic-resonance signal is sufficient, and the
 198 relaxation term can be omitted. Compared to the MRS method, the depth of the sensor in the
 199 borehole introduces an additional parameter that allows improving vertical resolution, and the
 200 kernel must be calculated considering each position of the sensor.

201 **Inverse modelling**

202 The MRS inverse problem can be considered as linear, and we approximate the integral
 203 equation of Eq. 5 by the matrix equation

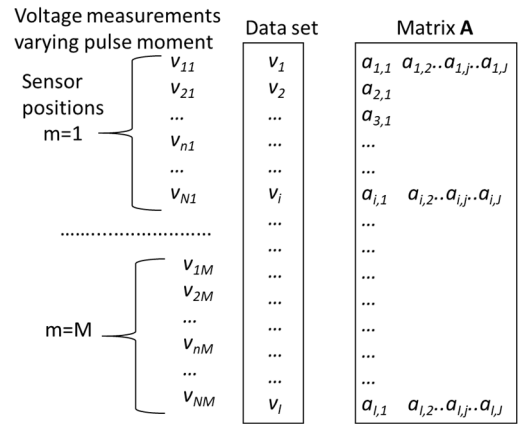
$$204 \quad \mathbf{A}\mathbf{w} = \mathbf{v} \quad , \quad (6)$$

205 where $\mathbf{v} = v_1, v_2, \dots, v_i, \dots, v_I$ is a set of experimental data, $\mathbf{w} = w_1, w_2, \dots, w_j, \dots, w_J$ is the solution
 206 vector and \mathbf{A} is a $I \times J$ matrix representing the kernel of Eq. 5.

207 We assumed a horizontal stratification (1-D inverse problem) and represented the
 208 subsurface by J homogeneous layers. Elements of the solution vector (w_j) represented the
 209 water content in corresponding layers. Elements of the data vector v_i included the voltage
 210 measured in the receiving coil at each sensor position *versus* pulse moment in the transmitting
 211 loop. The total number of measured points $I = \sum_{m=1}^M N_m$, where M is the number of sensor
 212 positions and N_m is the number of pulse moments, corresponding to position m . The matrix
 213 \mathbf{A} is built in accordance with the measuring procedure.

214 During our study, we set the sensor at one depth and made measurements for all pulse
 215 moments. Then, we changed the depth and repeated the measurements. Note that, compared
 216 to MRS, the measurements at each sensor position required fewer pulse moments. One may
 217 use only pulse moments corresponding to the maximum sensitivity around the sensor

218 position. Each element $a_{i,j}$ of matrix **A** was computed with Eq. 5 and contained the
 219 amplitude of the magnetic resonance signal corresponding to sensor depth and the value of
 220 pulse moment (Fig. 7).



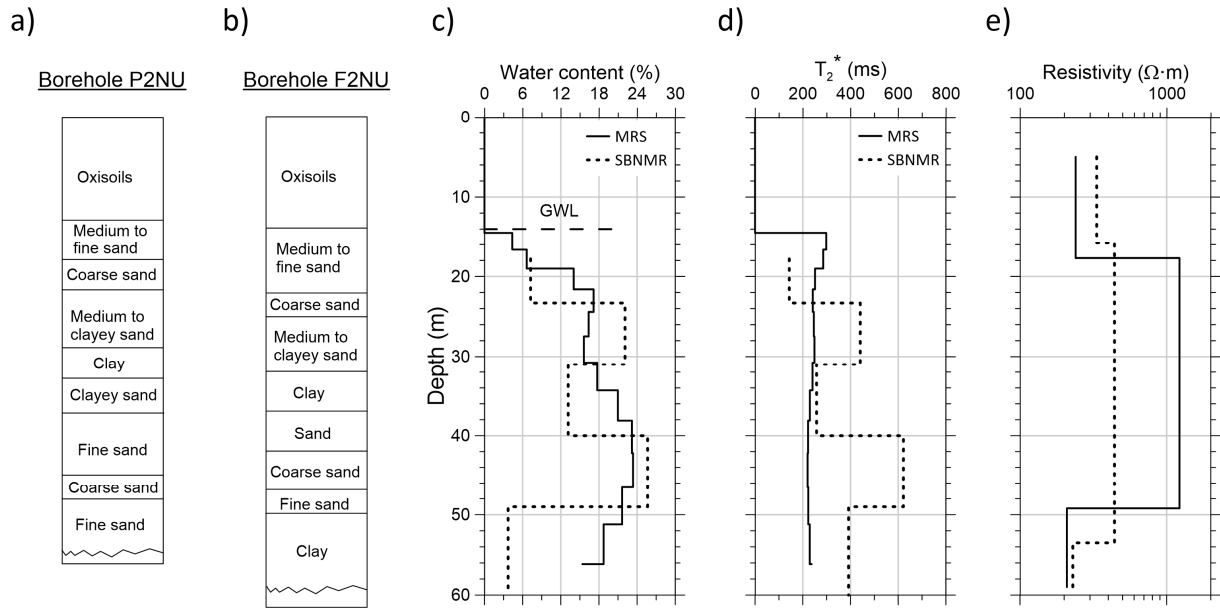
221
 222 *Fig. 7. SBNMR data prepared for inversion.*

224 We used the time-step inversion (Legchenko et al., 2002) based on the Tikhonov
 225 regularization method. Other existing algorithms, such as the QT inversion (Mueller-Petke
 226 and Yaramanci, 2010), are applicable as well.

227 **Field measurements**

228 For testing the SBNMR method, we performed measurements in the southern part of the
 229 Republic of Benin. The township of Abomey Calavi is located between the latitudes
 230 6°20'23.4" and 6°42'6.6" North, and the longitudes 2°14'13.8" and 2°25'7.8" East. At the
 231 Ouédo test site, the Tertiary “Continental Terminal” formation is rather irregular, but makes
 232 up a good aquifer (Hounsinou et al., 2014). It is composed of intercalations of fine to coarse
 233 sand layers with clay patterns (Lang et al., 1990) shown in Figs. 8a and 8b.

234



235

236

237

238

239

240

241

242

243

244

245

246

247

248

249

250

251

252

253

254

255

256

257

Fig. 8. a,b) Lithological logs of boreholes P2NU and F2NU used for SBNMR experiments. c) Water content distribution provided by MRS sounding (solid line) and by SBNMR measurements (dashed line). d) Corresponding relaxation time T_2^ . e) Electrical resistivity of the subsurface derived from TEM measurements (two equivalent models).*

The substratum of this aquifer is composed of continuous clay. The average depth of the substratum, as identified by 15 electrical soundings (VES), is 112 m (90 to 140 m) with an average resistivity of $64 \Omega \cdot m$ (between 200 and $30 \Omega \cdot m$). The aquifer formation has an average resistivity of $380 \Omega \cdot m$ (between 750 and $90 \Omega \cdot m$). Because of the relatively high electrical resistivity and small thickness, the clay layers within the aquifer formation were not resolved by 15 VES and 31 transient EM (TEM) soundings. The average borehole depth is 143 m (110 to 171 m).

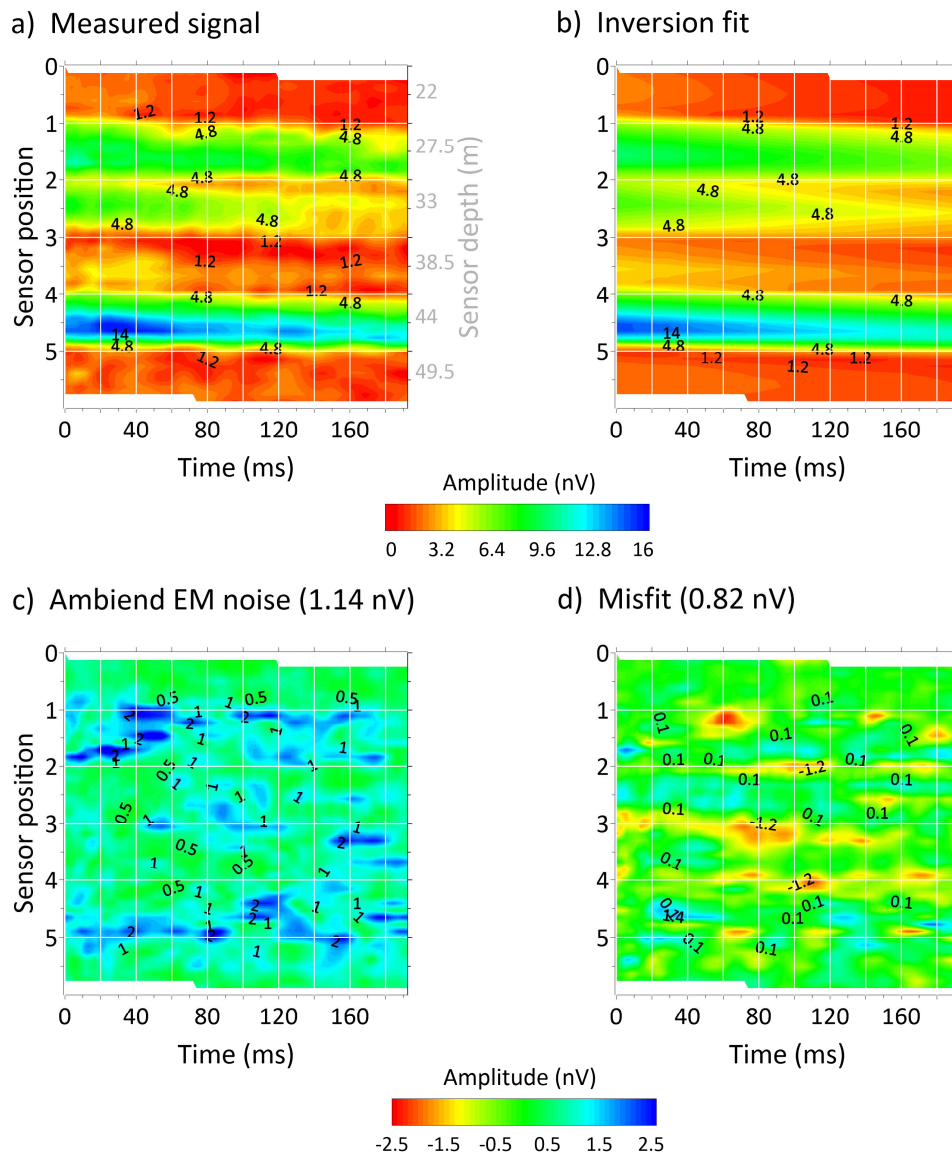
In the study area, the inclination of the Earth's magnetic field is $5^\circ N$ and the Larmor frequency is about 1393 Hz. For our study, we used a commercially available NUMIS^{poly} MRS instrument (Iris Instruments). The induction-coil sensor was placed in borehole F2NU (PVC casing) and the transmitting loop (25-m-side square, 3 turns) was laid out around it. Another borehole (P2NU) was located 10 m from F2NU. An MRS sounding with a coincident figure-eight square loop (62.5-m-side) was set up around borehole F2NU. The length of the cable connecting the instrument and the sensor was 50 m, which defined the deepest position of the sensor. The amplitude of the NMR signal measured with the downhole sensor is a function of both pulse moment and sensor depth. It has a typical for MRS a half-sinus-wave shape. We selected values of the pulse moment individually for each depth so that we always

258 observed a maximum SBNMR signal. To improve the signal to noise ratio (SNR), we used
259 stacking (usually close to 100). Logging data were not available for these boreholes and we
260 additionally carried out Transient EM (TEM) measurements using a TemFast-48 instrument
261 (AERM) with a coincident 100-m-side square loop. For interpreting the MRS measurements,
262 we used Samovar software (IRD) and for TEM data IX1D v.3.6 (Interpex). The SBNMR data
263 set was processed with experimental software developed by the authors. Figs. 8a and 8b show
264 the lithological logs of two boreholes, ten metres in-between and both located within the
265 transmitting loop. The core analysis shows that both boreholes intersected sand and clay
266 layers, but not at the same levels, demonstrating the lateral heterogeneity of the subsurface.
267 This heterogeneity was neither resolved by MRS sounding (Figs. 8c and 8d) nor by TEM
268 sounding (Fig. 8e). For the MRS and TEM measurements we used large loops and signals
269 from heterogeneous formations were thus averaged. SBNMR shows differences in water
270 content between three zones, but the resolution was insufficient for clearly distinguishing in-
271 between. The sensor was in borehole F2NU and both, high values of the water content (22
272 and 25%) and long relaxation time (440 and 622 ms) suggest two coarse sand layers (23-31 m
273 and 40-49 m). These layers are separated by a less permeable layer with the average water
274 content of 13% and the relaxation time of 258 ms (31-40 m), identified as clay and sand
275 formations. The correspondence between SBNMR and borehole results is not perfect, which
276 may be explained by the scale factor affecting both data sets. The lithological logs show
277 results corresponding to the layers intersected by the borehole and SBNMR provides
278 information averaged over the volume defined by sensor sensitivity.

279 Here, we present the SBNMR measurements with the sensor set at six different depths
280 from 22 to 49.5 m. Before stacking and filtering, the noise varied between 20 and 30 nV.

281 Fig. 9 shows the entire SBNMR data set used for inversion. For each position of the
282 downhole sensor, time series are recorded with a few different values of the pulse moment.
283 Each record consists of measuring ambient EM noise before the pulse and SBNMR signal
284 after the pulse. The dead time between the end of the pulse and the signal recording was 40
285 ms. Fig. 9a shows time records plotted versus time (0-192 ms) and sensor positions (0-5). The
286 right vertical axis (grey colour) shows the correspondence between the sensor position and the
287 depth of the top of the sensor. For each sensor position, time series are plotted considering
288 normalized pulse moments. For example, a record plotted at the sensor position 0 corresponds
289 to the minimum pulse moment, and the maximum pulse moment corresponds to the position 1
290 (left vertical axis). Corresponding ambient EM noise records are shown in Fig. 9c. Fig 9b
291 shows theoretical SBNMR signals computed after the inverse model; and Fig. 9d shows the

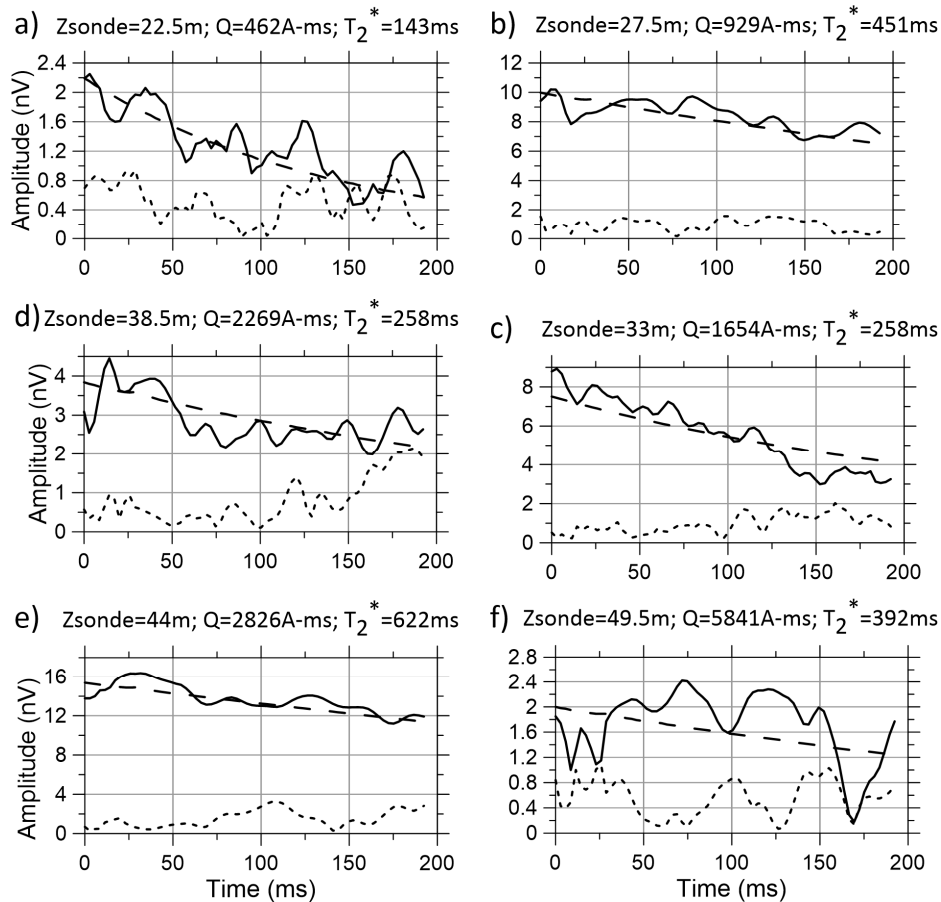
292 misfit between measured and theoretical signals. The misfit was computed as the root mean
 293 square error between experimental and theoretical time series.



294
 295
 296 *Fig. 9. a) Amplitude of SBNMR signal (colour scale) versus time (after the dead time)*
 297 *recorded at different sensor positions (left vertical scale). For each sensor position, the right*
 298 *vertical axis (grey colour) shows a depth corresponding to the sensor top. b) Theoretical*
 299 *signal computed after the inverse model. c) Noise records corresponding to the same time*
 300 *series. d) The misfit between measured and theoretical signals.*

301
 302 Fig. 10 shows time records extracted from the data shown in the previous figure. Each
 303 graph corresponds to one of the sensor positions. Solid lines show the envelope of the signal
 304 amplitude *versus* time and the dashed lines show the noise amplitude recorded before the

305 pulse. At all sensor positions, the SBNMR signal clearly dominates noise, thus confirming the
 306 feasibility of our SBNMR measurements. These examples also demonstrate pronounced
 307 differences between SBNMR signals recorded at different depths corresponding to different
 308 geological patterns. Theoretical signals computed after the inverse models fit measured data
 309 with the error of 0.82 nV and the mean noise was 1.14 nV.



310
 311 *Fig. 10. SBNMR records measured with the sensor located at different depths. Solid lines*
 312 *show the SBNMR signal recorded after the dead time following the pulse, long-dashed lines*
 313 *show inversion fits and short-dashed lines show noise records before the pulse.*

314
 315 **Discussion**

316 Our experimental study has confirmed the feasibility of surface-borehole NMR
 317 measurements. SBNMR is both similar and different compared to both MRS and borehole
 318 NMR, but provides information about groundwater unavailable with the last two methods.

319 Borehole NMR uses an artificial static magnetic field that allows a high sensitivity. The
 320 depth resolution of borehole NMR and the maximum depth of investigation are also much
 321 better than with SBNMR and MRS. However, borehole NMR investigates only a narrow zone
 322 around borehole, the sensitive area being located within the walls of a cylinder. The diameter

323 of this (virtual) cylinder (<40 cm) and the wall thickness (<2 mm) are determined by the
324 gradient of the static magnetic field (Dunn et al., 2002). Consequently, hydraulic parameters
325 of the aquifer formation investigated with borehole NMR should be considered as local data.
326 Additionally, some zone around the borehole can be modified by drilling, affecting the results
327 of the study. On the contrary, MRS and SBNMR provide data averaged over large
328 undisturbed volumes.

329 Operating in the geomagnetic field, MRS and SBNMR both have low sensitivity and a
330 poor signal-to-noise ratio. Results are averaged over a large investigated area that depends on
331 the size of the transmitting loop. SBNMR has better vertical resolution and a potentially
332 larger depth of investigation than MRS. It also better characterizes the investigated aquifer
333 formations in terms of geometry, porosity and hydraulic conductivity. Measurements of both
334 T_1 and T_2 are available with SBNMR as well as with MRS (Legchenko et al., 2004; 2010).

335 As we have shown the feasibility of this type of measurements, we think that our principal
336 goal was achieved.

337 **Conclusions**

338 We developed and successfully tested in a near-horizontal Earth's magnetic field a
339 borehole sensor for surface-borehole NMR investigations. SBNMR results are averaged over
340 the sensitive area of the sensor that spreads out to a few meters around the borehole.
341 Groundwater at up to 1 m around borehole does not produce a measurable SBNMR signal
342 because of the strong disturbance of the Earth's magnetic field by the magnetic core of the
343 sensor. Similar to MRS, the performance of SBNMR is site dependent and the inherently poor
344 signal-to-noise ratio is comparable to that of MRS.

345 **Acknowledgements**

346 This work was carried out in the framework of a collaboration agreement between IRD,
347 IRIS Instruments and BRGM. The authors acknowledge financial support provided by grants
348 from the French national programmes Labex OSUG@2020 (Investissements d'avenir –
349 ANR10 LABX56) and the “Investment for Future - Excellency Equipment” project
350 EQUIPEX CRITEX (grant #ANR-11-EQPX-0011). Field data in Benin were obtained as part
351 of the GRIBA project funded by the African Union, the European Union, and IRD (grant
352 AURG/098/2012). The authors acknowledge contributions of two anonymous reviewers
353 helping us to prepare this paper. We thank Dr H.M. Kluijver edited the final English version
354 of the MS.

355 The content of this paper is the responsibility of the authors and cannot be regarded as
356 reflecting the position of the European Union or the African Union.

357 **References**

358 Behroozmand, A.A., Keating, K., Auken, E., 2015. A review of the principles and
359 applications of the NMR technique for near-surface characterization. *Surv. Geophys.*,
360 36(1), 27-85, doi: 10.1007/s10712-014-9304-0.

361 Chevalier, A., Legchenko, A., Girard, J.F., Descloitres, M., 2014. 3D Monte Carlo inversion
362 of magnetic resonance measurements. *Geophys. J. Intern.*, 198(1), 216-228, doi:
363 10.1093/gji/ggu091.

364 Clément, R., Legchenko, A., Quetu, M., Descloitres, M., Oxarango, L., Guyard H., Girard,
365 J.F., 2011. Experimental study of a domestic waste material using magnetic resonance
366 measurements. *Near Surf. Geophys.*, 9, 179-185, doi: 10.3997/1873-0604.2010069.

367 Davis, A.C., Dlugosch, R., Queitsch, M., Macnae, J.C., Stolz, R., Müller-Petke, M., 2014.
368 First evidence of detecting surface nuclear magnetic resonance signals using a compact B-
369 field sensor, *Geophys. Res. Lett.*, 41, 4222–4229, doi:10.1002/2014GL060150.

370 Dunn, K.J., Bergman, D.J., Latorraca, G.A., 2002. *Nuclear Magnetic Resonance*
371 *Petrophysical and Logging Applications*. Elsevier Science Ltd, UK.

372 Girard, J-F, Boucher, M., Legchenko, A., Baltassat, J.M., 2007. 2D magnetic resonance
373 tomography applied to karstic conduit imaging. *J. Appl. Geophys.*, 63, 103-116, doi:
374 10.16/j.jappgeo.2007.08.0001.

375 Grombacher, D., Liu, L., Larsen, J.J., Auken, E., 2018. Practical considerations for small
376 receive coils in surface NMR. *J. Appl. Geophys.*, 154, 81-92, doi:
377 10.1016/j.jappgeo.2018.04.005.

378 Hertrich, M., Braun, M., Yaramanci, U., 2005. Magnetic resonance soundings with separated
379 transmitter and receiver loops. *Near Surf. Geophys.*, 3(3), 131–144, doi:10.3997/1873-
380 0604.2005010.

381 Hertrich, M., 2008. Imaging of groundwater with nuclear magnetic resonance. *Prog. Nucl.*
382 *Magn. Reson. Spectrosc.*, 53(4), 227–248, doi:10.1016/j.pnmrs.2008.01.002.

383 Hertrich, M., Green, A.G., Braun, M., Yaramanci, U., 2009. High-resolution surface-NMR
384 tomography of shallow aquifers based on multi-offset measurements. *Geophysics*, 74,
385 G47-G59, doi:10.1190/1.3258342.

386 Hounsinou, P., Mama, D., Alassane, A., Boukari, M., 2014. Hydrogeology and Chemistry
387 Synthesis of the deep Boring of the Township of Abomey-Calavi, Benin. *Res. J. Chem.*
388 *Sci.*, 4(12), 98-102.

389 Lang, J., Kogbe, C., Alidou, S., Alzouma, K.A., Bellion, G., Dubois, D., Durand, A., Guiraud,
390 R., Houessou, A., de Klasz, I., Romann, E., Salard-Chebouldaëff, M., Trichet, J., 1990. The
391 Continental Terminal in West Africa. *J. Afr. Earth Sci.*, 10(1-2), 79-99, doi: 10.1016/0899-
392 5362(90)90048-J.

393 Legchenko, A.V., Beauce, A., Guillen, A., Valla, P., Bernard, J., 1997. Natural variations in
394 the magnetic resonance signal used in PMR groundwater prospecting from the surface.
395 *Eur. J. Environ. Eng. Geophys.*, 2, 173-190.

396 Legchenko, A., Valla, P., 2002. A review of the basic principles for proton magnetic
397 resonance sounding measurements. *J. Appl. Geophys.*, 50, 3–19., doi: 10.1016/S0926-
398 9851(02)00127-1.

399 Legchenko, A., Baltassat, J.M., Beauce, A., Bernard, J., 2002. Nuclear magnetic resonance as
400 a geophysical tool for hydrogeologists. *J. Appl. Geophys.*, 50, 21-46, doi:10.1016/S0926-
401 9851(02)00128-3

402 Legchenko, A., Baltassat, J.M., Bobachev, A., Martin, C., Robin, H., Vouillamoz, J.M., 2004.
403 Magnetic resonance sounding applied to aquifer characterization. *J. Ground Water*, 42(3),
404 363–373, doi: 10.1111/j.1745-6584.2004.tb02684.x.

405 Legchenko, A., Vouillamoz, J.M., Roy, J., 2010. Application of the magnetic resonance
406 sounding method to the investigation of aquifers in the presence of magnetic materials.
407 *Geophysics*, 75(6), L91–L100, doi: 10.1190/1.3494596.

408 Legchenko, A., 2013. *Magnetic Resonance Imaging for Groundwater*. Wiley-ISTE 978-1-
409 84821-568-9.

410 Legchenko A., Pierrat, G., 2014. Glimpse into the design of MRS instrument. *Near Surf.*
411 *Geophys.*, 12, 297 – 308, doi:10.3997/1873-0604.2014006.

412 Legchenko, A., Miège, C., Koenig, L.S., Forster, R.R., Miller, O., Solomon, D.K., Schmerr,
413 N., Montgomery, L., Ligtenberg, S., Brucker, L., 2018. Estimating water volume stored in
414 the south-eastern Greenland firn aquifer using Magnetic-Resonance Soundings. *J. Appl.*
415 *Geophys.*, 150, 11–20, doi: 10.1016/j.jappgeo.2018.01.005.

416 Müller-Petke M., Yaramanci, U., 2008. Resolution studies for Magnetic Resonance Sounding
417 (MRS) using the singular value decomposition. *J. Appl. Geophys.*, 66, 165–175, doi:
418 10.1016/j.jappgeo.2007.11.004.

419 Mueller-Petke, M., Yaramanci, U., 2010. QT inversion — Comprehensive use of the
420 complete surface NMR data set. *Geophysics*, 75, 4, WA199–WA209, doi:
421 10.1190/1.3471523.

422 Müller-Petke, M., Hiller, T., Herrmann, R., Yaramanci, U., 2011. Reliability and limitations
 423 of surface NMR assessed by comparison to borehole NMR. *Near Surf. Geophys.*, 9, 123–
 424 34, doi: 10.3997/1873-0604.2010066.

425 Parsekian, A.D., Grombacher, D., 2015. Uncertainty estimates for surface nuclear magnetic
 426 resonance water content and relaxation time profiles from bootstrap statistics. *J. Appl.*
 427 *Geophys.* 119, 61–70, doi: 10.1016/j.jappgeo.2015.05.005.

428 Stoeffl, W., 2001. Use of earth field spin echo NMR to search for liquid minerals. Patent N°
 429 US 6,177,794 B1.

430 Tumanski, S., 2007. Induction coil sensors—a review. *Meas. Sci. Technol.* 18, R31–R46, doi:
 431 10.1088/0957-0233/18/3/R01.

432 Walsh, D., Turner, P., Grunewald, E., Zhang, H., Butler, J.J.Jr., Reboulet, E., Knobbe, S.,
 433 Christy, T., Lane, J.W. Jr., Johnson, C.D., Munday, T., Fitzpatrick, A., 2013. A small-
 434 diameter NMR logging tool for groundwater investigations. *J. Ground Water*, 51(6), 914–
 435 926, doi:10.1111/gwat.12024.

436 Weichman, P.B., Lavelly, E.M., Ritzwoller M.H., 2000. Theory of surface nuclear magnetic
 437 resonance with applications to geophysical imaging problems, *Phys. Rev. E*, 62(1), 1290–
 438 1312, doi:10.1103/PhysRevE.62.1290.

439

440 **Figure captions**

441 *Fig. 1. Transmitting loop on the surface (Tx) and the induction-coil sensor downhole (Rx)*

442 *Fig. 2. Design of the borehole sensor (l_c – length of the core, D_c – diameter of the core, A_c*
 443 *– area of the core)*

444 *Fig. 3a) The resultant magnetic permeability of the core versus core diameter computed*
 445 *considering different core lengths ($\mu_r=2300$). b) The effective area versus core diameter*
 446 *($\mu_r=2300$). c) The effective area computed considering different magnetic-permeability values*
 447 *of the material and fixed core length ($l_c=0.94$ m).*

448 *Fig. 4. The experimental setup for measuring parameters of the induction-coil sensor*

449 *Fig. 5. Relaxation time T_2^* (left vertical axis) and Larmor frequency (right vertical axis)*
 450 *versus distance between sensor and water sample.*

451 *Fig. 6. Normalized amplitude of the test signal measured at different positions of the*
 452 *transmitting coil versus distance between sensor and coil. Dashed lines show the power fit of*
 453 *experimental data.*

454 *Fig. 7. SBNMR data prepared for inversion.*

455 *Fig. 8. a,b) Lithological logs of boreholes P2NU and F2NU used for SBNMR experiments.*
456 *c) Water content distribution provided by MRS sounding (solid line) and by SBNMR*
457 *measurements (dashed line). d) Corresponding relaxation time T_2^* . e) Electrical resistivity of*
458 *the subsurface derived from TEM measurements (two equivalent models).*

459 *Fig. 9. a) Amplitude of SBNMR signal (colour scale) versus time (after the dead time)*
460 *recorded at different sensor positions (left vertical scale). For each sensor position, the right*
461 *vertical axis (grey colour) shows a depth corresponding to the sensor top. b) Theoretical*
462 *signal computed after the inverse model. c) Noise records corresponding to the same time*
463 *series. d) The misfit between measured and theoretical signals.*

464 *Fig. 10. SBNMR records measured with the sensor located at different depths. Solid lines*
465 *show the SBNMR signal recorded after the dead time following the pulse, long-dashed lines*
466 *show inversion fits and short-dashed lines show noise records before the pulse.*

467